High-Efficiency Multispectral-Polarization Imaging System Using Polarization Camera Array With Notch Filters

Feng Huang, Rongjin Cao, Peng Lin, Bin Zhou, and Xianyu Wu

***Abstract*— Incident light captured by an optical imaging system engenders multidimensional high-level optical information, such as spatial resolution, light intensity, spectrum, and polarization. However, panchromatic image sensors can only capture spatial and light intensity information. This article presents a novel multispectral-polarization imaging approach that overcomes the limitations related to low light flux and slow imaging speed found in multispectral-polarization techniques based on bandpass filters. By utilizing notch filters and a camera array and integrating computational imaging algorithms, this method achieves high temporal, spatial, and spectral resolution in polarization imaging for the first time. The spatial, light intensity, spectral, and polarization information of the target scene can be obtained synchronously while guaranteeing high light efficiency performance of the system. To obtain high spectral resolution polarization images, a K-times singular value decomposition (K-SVD) algorithm is used to extract the feature dictionary of the hyperspectral dimension. Then, a compressive sensing-based algorithm is applied to conduct spectral super-resolution. The principle of compressive sensing is combined with prior sparsity and smoothness information to perform spectral super-resolution. The performance of the proposed multispectral-polarization imaging system and the effectiveness of the proposed method were verified using a public multispectral dataset and field experiments. The experimental results confirm that the proposed technology can obtain high-quality spatial resolution, light intensity, spectral, and polarization data of the target scene in a single shot. The algorithm can reconstruct 16 spectral band images from four captured spectral images while adequately preserving the polarization information of the target scene in the calculated spectral imaging results.**

***Index Terms*— Compressive sensing, multicamera imaging, multispectral computational imaging, multispectral-polarization imaging, notch filters.**

I. Introduction

CAPTURING high-resolution multidimensional optical information using 2-D image sensors has attracted growing attention in the field of remote sensing. While intensity, frequency, wavelength, and polarization constitute the main properties of the light captured by an imaging system, light polarization has a particular advantage. In fact, 2-D imaging of the polarization information enables the characterization of the microstructure and surface roughness of the imaged target. Nonetheless, the spectral information of the target provides signatures of its absorption, reflection, or refraction characteristics [1]. Therefore, a combined and synchronized acquisition of both polarization and spectral information (i.e., spectral-polarization data) can enable fast and highly accurate target recognition and classification. Thus, multispectral-polarization imaging techniques hold particularly interesting potential applications in various fields, including satellite remote sensing [2], [3], medical diagnosis [4], target identification [5], etc.

Nonetheless, existing multispectral-polarization remote sensing imaging systems suffer from several drawbacks. For instance, the polarization and directionality of the Earth reflectance [2] and the directional polarimetric camera [6] adopt a rotating filter wheel to switch between different polarization and spectral filters by controlling the wheel angle. This approach infers poor synchronization and real-time imaging performance, which is limited by the rotating speed of the wheel. Furthermore, the Aerosol Polarimeter Sensor [3] and Multiangle SpectroPolarimetric Imager [7] use the division of amplitude technique to guide light into different channels fitted with polarizers or filters. Their imaging speed and light efficiency are limited by the light-blocking elements and complex optical path design. Recently, a biomimetic multispectral-polarization imaging technique with better real-time performance, inspired by the compound eye visual system of insects, has gradually emerged as an attractive research field [8], [9].

The conventional multispectral-polarization imaging technique combines the division of time spectral and time polarization imaging systems, such as an integrated bandpass filter wheel and rotating polarizer, for data acquisition. Polarization imaging techniques use either a combination of a 2-D image sensor with a polarizer or an array of pixelated micropolarizers to capture 3-D optical information. Polarization imaging methods can be classified, depending on the modulation of polarization, into division-of-time, division-of-amplitude, division-of-aperture, and division-of-focal-plane [10], as shown in Table I. The division-of-time method [11] obtains the polarization information of target scenes by rotating the polarizer or wave plate. This technique leads to poor real-time performance and is unsuitable for dynamic imaging. For instance, certain multispectral and polarization

Manuscript received 10 April 2023; revised 26 September 2023; accepted 9 October 2023. Date of publication 30 October 2023; date of current version 8 November 2023. This work was supported in part by Fuzhou University under Grant GXRC-18066 and in part by the Natural Science Foundation of Fujian Province of China under Grant 2023J01130137. The Associate Editor coordinating the review process was Dr. Md. Moinul Hossain. *(Corresponding author: Xianyu Wu.)*

The authors are with the School of Mechanical Engineering and Automation, Fuzhou University, Fuzhou 35018, China (e-mail: xwu@fzu.edu.cn).

Digital Object Identifier 10.1109/TIM.2023.3328697

imaging systems [12], [13], [14] utilize rotating polarizers, quarter-wave plates, and custom illumination units to precisely capture the polarization state and spectral images of subjects or specimens. The division-of-amplitude method [15] uses light splitters and polarizers of different angles in the optical path to obtain polarization information. However, as the number of beam splitters increases, the amount of light passing through each channel decreases, which degrades the imaging quality. For instance, Liu et al. [16] devised an innovative simultaneous polarization and multispectral imaging system with a common aperture, covering visible, mid-wave infrared, and long-wave infrared wavebands, and integrated division-of-focal-plane and division-of-aperture-plane polarimeters for real-time polarization imaging, thus enhancing its capability in detecting and identifying low-contrast targets across various imaging scenarios. In the division-of-aperture method [17], multiple subapertures with different polarizers or wave plates share a focal plane detector array. This approach provides excellent synchronization and real-time performance but is strongly restricted in terms of spatial resolution. The division-of-focal-plane method [18] uses integrated circuit manufacturing techniques to place a micropolarization array in front of the focal plane detector array, which enables simultaneous and synchronous real-time imaging of multiple polarization states of the target scene. Shinoda and Ohtera [19] introduced a novel Voronoi-structure-based photonic crystal filter and a method for creating a snapshot multispectral-polarization camera. This approach allows for filter attachment without the need for specific alignment and enables the simultaneous capture of spectra, linear polarization, and RGB images from a single exposure. Shinoda et al. [20] introduced a novel multispectral-polarization filter array and demosaicking method for snapshot multispectral-polarization imaging, and they demonstrate the approach's ability to recover spectral information and generate diverse polarized and non-polarized RGB images through experiments.

In addition, methods for acquiring spectral data cubes using 2-D image sensors should be developed to extend the capabilities of existing spectral imaging techniques. A conventional spectral imaging system can acquire spectral data either by scanning or snapshot imaging. Scanning imaging includes point, line, and wavelength scanning. However, these methods are time-consuming and inapplicable to dynamic imaging due to the difficulty of synchronizing images in different bands. Thus, the demand for dynamic spectral imaging has promoted the development of snapshot spectral imaging techniques. For example, CSMUP [21] can achieve single-shot real-time ultrafast imaging with an approximate rate of 250 billion frames per second. According to the different imaging approaches, snapshot spectral imaging is mainly classified into coded aperture imaging, division-of-aperture, and division-of-focal-plane methods [22]. If the number of spectral bands that can be acquired directly by snapshot spectral imaging is small, computational imaging methods are used. These include spectral super-resolution methods based on compressed sensing or deep learning for improving the spectral resolution of the acquired data. Commonly used spectral super-resolution methods include neural networks [23], principal component analysis [24], non-negative matrix decomposition [25], [26], and compressive sensing [27]. It is worth noting that existing methods have been able to recover multispectral data from RGB images only in specific scenarios [23], [28], [29]. Nonetheless, the computational reconstruction process of spectral images remains a challenge. Previous research results showed that adding panchromatic image data to the solution process can reduce the uncertainty and improve the quality of reconstructed images.

Furthermore, compared to spectral imaging systems based on bandpass filters, those implementing notch filters can achieve higher light pass efficiency and provide richer spectral information. Preliminary research results demonstrate that, in some scenarios, notch filters can achieve higher signal-to-noise ratios (SNRs) compared to bandpass filters [30]. Additionally, the system's performance is enhanced when using a notch filter for spectral [24] and night-vision imaging [31].

Existing multispectral-polarization imaging systems based on bandpass filters have limitations in ensuring high performance in terms of both light efficiency and resolution, i.e., they cannot achieve high spatial, temporal, and spectral resolution simultaneously. To extend the application of notch-filter-based single-lens multispectral cameras [24] to the field of multispectral-polarization imaging, this study uses notch filters and a polarization imaging sensor array to construct a multiaperture multispectral-polarization imaging system. The proposed imaging system resolves the problems of low light efficiency and light-blocking elements in the optical path, which can negatively affect the imaging quality, exposure time, and imaging speed of existing multispectral-polarization imaging systems. Moreover, we have developed a spectral super-resolution algorithm and combined it with our proposed system to obtain high-quality multispectral-polarization imaging results.

Distinct from the notch spectral imaging systems based on a nine-aperture camera array as presented in [1] and [31], this article introduces a further simplification of the imaging system structure. Utilizing notch filters and polarization imaging cameras, a four-aperture polarization camera array is established for spectral-polarization imaging. The influence of different combinations of notch filters on computed reconstructed spectral images is assessed, and a specialized algorithm for reconstructing polarization spectral images is introduced.

Therefore, a high-efficiency multispectral-polarization imaging system combining the advantages of notch filters and polarization imaging sensors is proposed and demonstrated. The effectiveness of the system and method is verified using public simulation datasets and field experiments. The simulation and experimental results confirm that the prototype system and method proposed can acquire information of the target from 16 spectral bands and four polarization states simultaneously. The proposed approach is further compared with data collected by a polarized camera equipped with a bandpass filter.

TABLE I
COMPARISON IMAGING POLARIMETRY METHODS

Methods	Advantages	Disadvantages
Division of Time [11-14]	Accurate polarization information measurement; simple imaging system design.	Obtains polarization information by rotating the polarizer or wave plate; resulting in poor real-time performance and unsuitability for dynamic imaging.
Division of Amplitude [12 16]	Simultaneous acquisition of multiple high-resolution polarization images; suitable for capturing dynamic scenes.	Restricted imaging speed due to low light efficiency; multiple focal plane arrays require complex circuit systems for image synchronization; complex image registration algorithms are required.
Division of Aperture [17]	Compact Structure; Simultaneous acquisition of multiple polarization images with excellent real-time imaging performance; suitable for capturing dynamic scenes.	Limited imaging resolution, sub-images have disparities; image registration algorithms are required; not suitable for imaging objects up close due to Parallax issue.
Division of Focal Plane [14 19-20]	Simultaneous acquisition of multiple high-resolution polarization images with excellent real-time imaging performance; small size, low weight, and low power cost; suitable for capturing dynamic scenes.	Introduction of iFOV error due to the design of the micro polarizer mosaic array; demosaicing algorithms are required.

II. SYSTEM PRINCIPLES

A. System Imaging Model

The multispectral-polarization imaging system proposed in this study features the advantages of three techniques. Namely, notch filter-based spectral imaging, multiaperture imaging, and division of focal plane polarization imaging. Thus, this combined system enables the synchronous acquisition of the target's space (x, y), spectral (λ), and polarization (p) information. The principle of operation of this system is given as follows. First, the natural light $L(x, y, \lambda, p)$ reflected by the target passes through the ith notch filter for wavelength modulation $T_i(\lambda)$. Then, it enters the micropolarizer array for polarization modulation $\emptyset_j(p)$, where j represents the jth polarization direction (i.e., 0°, 45°, 90°, and 135°). The intensity value I measured by the image sensor is expressed by (1). The multispectral-polarization imaging principle is shown in Fig. 1

$$I_{i,j}(x, y, \lambda, p) = L(x, y, \lambda, p)T_i(\lambda)\phi_j(p). \tag{1}$$

B. Light Efficiency Analysis

The quality of the captured images is affected by the light throughput of the multispectral or polarization imaging systems, which is limited by the presence of light-blocking elements in the optical path. Assuming that there are N bands in the spectral range $[\lambda_0, \lambda_1]$, the conventional multiaperture multispectral imaging system using a bandpass filter has a light efficiency of $\sim 1/N$ like in a thin observation module by bound optics (TOMBO) [32]. In contrast, computational spectral imaging systems use coded masks to modulate the target information collected by a single aperture. Hence, the light efficiency in this case is mainly limited by the weight of the mask, which is $\sim 1/2$ in most cases, like in a coded aperture snapshot spectral imager (CASSI) [33]. It is worth noting that the light transmission efficiency is reduced in a spectral imaging system due to the use of bandpass filters. Similarly, the use of polarizers or micropolarizer arrays results in a reduction of the light transmission efficiency in a polarization imaging system. Therefore, the imaging quality and speed of the spectral-polarization imaging system are degraded by the low-pass light efficiency. Moreover, the low SNR of collected spectral images induces significant difficulties for postprocessing or computational imaging algorithms in computational spectral imaging technology. To overcome this difficulty and build a spectral-polarization imaging system with highly improved light throughput and reduced requirements for the spectral super-resolution algorithm, we propose using a notch filter instead of a bandpass filter.

Generally, for a notch filter and a bandpass filter with the same center wavelength and full-width at half-maximum, the light efficiency of the notch filter is $(N - 1)$ times that of the bandpass filter. Therefore, the notch filter can significantly reduce the exposure time and improve the frame rate of the imaging system. Fig. 2 shows a comparison of the imaging of a checkboard captured by a monochromatic camera covered with either a notch filter (532 nm) or a bandpass filter (530 nm) under the same light conditions. As indicated, to obtain similar imaging results, the exposure time of the bandpass filter imaging system had to be as high as 120 000 μs, whereas that of the notch filter imaging system was only 4000 μs, i.e., the frame rate when using a notch filter was 30 times higher than when using a bandpass filter.

Ideally, the transmittance of a bandpass filter $T_i(\lambda)$ and that of a notch filter $\hat{T}_i(\lambda)$ can be expressed as (2) and (3), respectively

$$T_i(\lambda) = \begin{cases} 1, & |\lambda - \lambda_i| < b/2 \\ 0, & \text{otherwise} \end{cases}, \quad i = 1, 2, \ldots, N \tag{2}$$

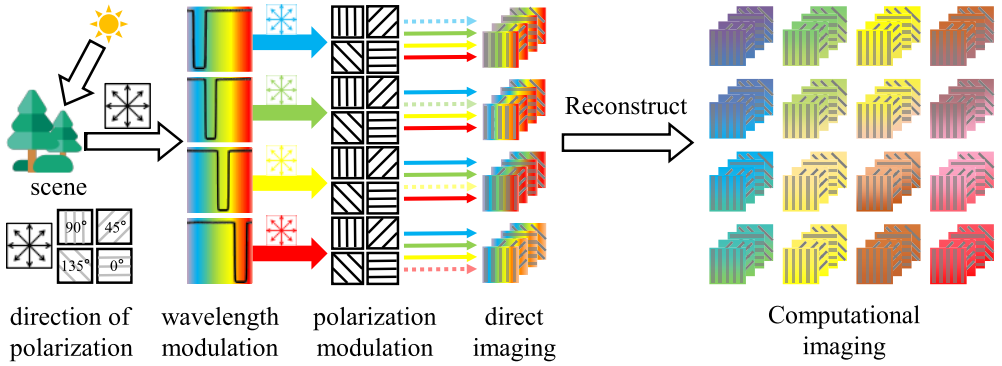

Fig. 1. Schematic of the multispectral-polarization imaging system.

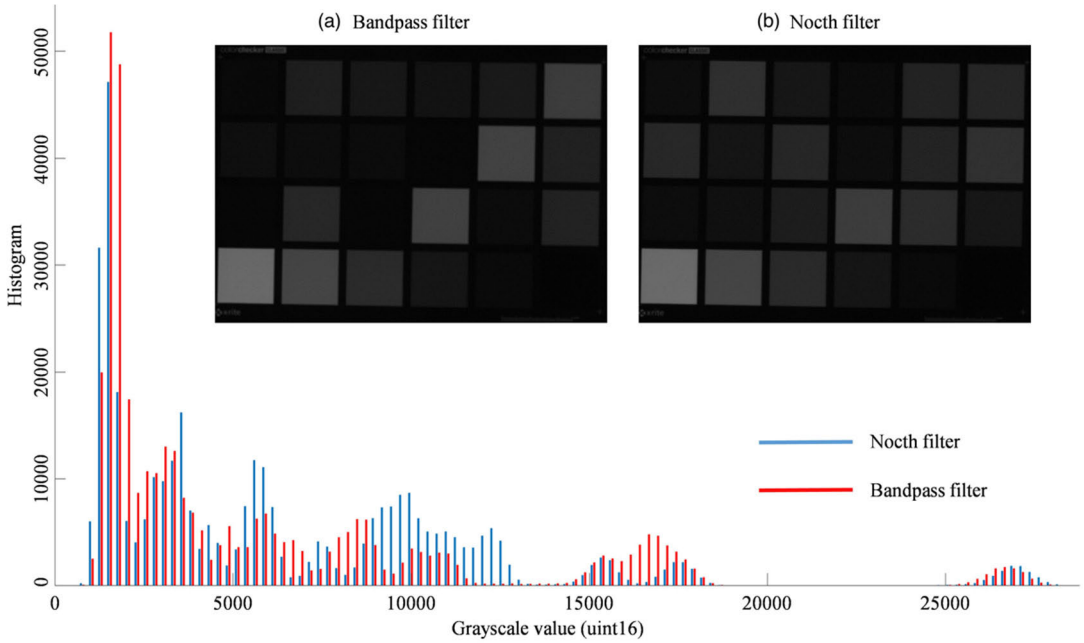

Fig. 2. Comparison of histograms of the imaging results captured by a monochromatic camera with (a) bandpass filter, exposure time 120 000 μs (8.333 fps), and (b) notch filter, exposure time 4000 μs (250 fps).

$$\hat{T}_i(\lambda) = \begin{cases} 1, & |\lambda - \lambda_i| > b/2 \\ 0, & \text{otherwise} \end{cases} = 1 - T_i(\lambda), \quad i = 1, 2, \ldots, N \tag{3}$$

where $\lambda_i = \lambda_0 + ib$ is the central wavelength of the ith notch filter. The ideal bandwidth of the optical filter [30] is given by $b = (\lambda_1 - \lambda_0)/N$.

Given the quantum efficiency $Q(\lambda)$ of a camera and the original amount of light entering it $S(\lambda)$, the light intensity of the corresponding wavelength on a single pixel using either a bandpass or a notch filter can be calculated using (4) and (5), respectively

$$P_i = \int_{\lambda_0}^{\lambda_1} Q(\lambda) T_i(\lambda) S(\lambda) d\lambda \tag{4}$$

$$\hat{P}_i = \int_{\lambda_0}^{\lambda_1} Q(\lambda) \hat{T}_i(\lambda) S(\lambda) d\lambda = \int_{\lambda_0}^{\lambda_1} Q(\lambda)(1 - T_i(\lambda)) S(\lambda) d\lambda. \tag{5}$$

Without using any optical filter, the light intensity of the same pixel is given by

$$P_{\text{all}} = \int_{\lambda_0}^{\lambda_1} Q(\lambda) S(\lambda) d\lambda. \tag{6}$$

According to (4)–(6), the light intensity obtained by the camera at a given pixel through the notch filter can be expressed as

$$\hat{P}_i = P_{\text{all}} - P_i. \tag{7}$$

C. Spectral Super-Resolution

The light efficiency directly affects the maximum temporal resolution of the imaging system. Therefore, the time, spatial, and spectral resolutions should be considered in the design of a spectral-polarization imaging system. In this study, a multi-aperture imaging architecture is used to meet the time and spatial resolution requirements. A spectral super-resolution imaging algorithm based on a compressive sensing principle was used to improve the spectral resolution. The entire process

Fig. 3. Four-aperture snapshot multispectral-polarization imaging prototype built in this study. (a) and (b) Appearance of the prototype system. (c) Schematic diagram of notch filter installation.

of spectral super-resolution can be divided into two steps. First, the features of the spectral dimension were extracted, and then, the corresponding sparse matrix was solved. Prior information, such as low-rank [34], spectral smoothness [24], sparsity [35], and spatial–spectral correlation [36], is usually added to the solving process to improve the accuracy of the results. Combined use of different priors can improve the deficiency caused when using only a single prior. Here, sparsity and spectrum smoothness were introduced to make the restored spectral curve smoother.

Studies have proved that the intensity of each pixel in a natural scene can be expressed as a linear combination of spectral bases [24]. In our study, the spectral basis referred to a dictionary. The hyperspectral data of a pixel point (x, y) in the image $\boldsymbol{F} \in \mathbb{R}^{\mathrm{K}\times 1}$ are expressed as

$$\boldsymbol{F} = \boldsymbol{D}\boldsymbol{B} \tag{8}$$

where $\boldsymbol{D} \in \mathbb{R}^{K\times\Theta}$ represents the dictionary, K represents the number of spectral bands, $\boldsymbol{B} \in \mathbb{R}^{\Theta\times 1}$ is the corresponding sparse matrix, and Θ represents the number of atoms in the dictionary. To improve their performance, this study used complete dictionaries $\Theta = 4\mathrm{K}$.

Equation (9) defines the spectral data $\boldsymbol{Y} \in \mathbb{R}^{\theta\times 1}$ obtained by the imaging system, $\theta < \Theta$

$$\boldsymbol{Y} = \boldsymbol{H}\boldsymbol{F} = \boldsymbol{H}\boldsymbol{D}\boldsymbol{B} \tag{9}$$

where $\boldsymbol{H} \in \mathbb{R}^{\Theta\times K}$ represents the sampling matrix of the imaging system. In this work, $\boldsymbol{H}$ depended on the combination of the notch filter array and the transmittance of each notch filter.

Combining the prior information of image sparsity, (10) was solved to obtain the hyperspectral data $\boldsymbol{F}$

$$\arg\min_{\boldsymbol{B}} \|\boldsymbol{Y} - \boldsymbol{H}\boldsymbol{D}\boldsymbol{B}\|_{\mathrm{F}}^2 + \mu\|\boldsymbol{B}\|_1. \tag{10}$$

Here, $\|\cdot\|_{\mathrm{F}}$ represents the Frobenius norm, $\|\cdot\|_1$ represents the 1-norm, and μ is the regularization coefficient.

To improve the solution accuracy, a spectral smoothness constraint is introduced and the optimization equation becomes

$$\arg\min_{\boldsymbol{B}} \|\boldsymbol{Y} - \boldsymbol{H}\boldsymbol{D}\boldsymbol{B}\|_{\mathrm{F}}^2 + \mu\|\boldsymbol{B}\|_1 + \gamma\left\|\frac{\partial^2(\boldsymbol{D}\boldsymbol{B})}{\partial\lambda^2}\right\|_F^2. \tag{11}$$

The alternating direction method of multipliers [37] was used to solve (11). Finally, the hyperspectral data $\boldsymbol{F}$ were obtained.

D. System Implementation

The proposed multispectral-polarization imaging system based on notch filters and a four-aperture structure is shown in Fig. 3. The system comprises a notch filter array (Edmund OD 4.0 Nocth/Chroma ZET NF), lens array (Edmund 85869, FL 35mm, $f/1.8$–$f/16$), and polarizing camera array (FLIR BFS-U3-51S5P-C). The transmittance of the notch filters with different central wavelengths on the front cover of different apertures is shown in Fig. 4. A synchronous acquisition program was used to record the polarization images and video data. The compressive sensing approach described in Section II-C was applied to conduct spectral super-resolution with polarization information. As a result, the light intensity, multispectral, and polarization information of the target could be simultaneously obtained in a single shot. The notch filter images directly collected by the system required image registration preprocessing due to the differences in the field of view between each subaperture in the multiaperture imaging system. Because there was no obvious difference in brightness among the notch filter images, image registration could be performed using the SURF [38] algorithm and homography matrix transformation. The images acquired by the polarization imaging sensors were first decomposed into four images with different polarization states. Image registration was then performed for images in the same polarization states. In addition, since the imaging system is designed for long-distance imaging, a high overlapping rate of the images captured by different cameras and high image registration accuracy could be guaranteed, as shown in Fig. 5.

E. Calculation of Polarization Information

Our multiaperture imaging system was built by applying an array of division-of-focal-plane polarization cameras, which can capture four polarization states (i.e., 0°, 45°, 90°, and 135°), improving the real-time performance of polarization imaging. The angle of polarization (AoP) and degree of linear polarization (DoLP) of the target can be obtained from (12)

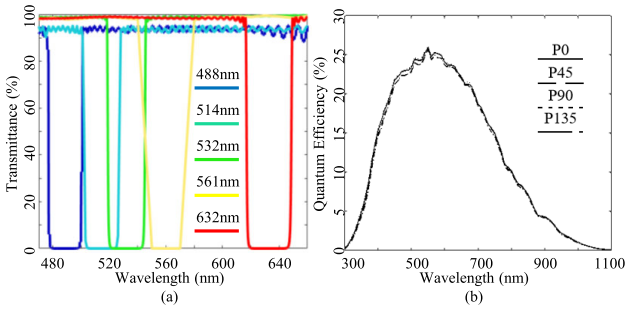

Fig. 4. (a) Transmittance of notch filters with central wavelengths of 488, 514, 532, 561, and 632 nm. (b) Quantum efficiency of polarization imaging sensors used in this study.

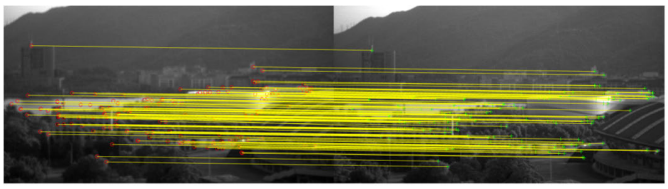

Fig. 5. Feature point pairs matched between two images acquired through two different subapertures under the same polarization states.

and (13), respectively [39]

$$\text{AoP} = \frac{1}{2}\arctan\left(\frac{S_2}{S_1}\right) \tag{12}$$

$$\text{DoLP} = \frac{\sqrt{S_1^2 + S_2^2}}{S_0} \tag{13}$$

where S_0, S_1, and S_2 are known as the Stokes parameters defined by (14)–(16). $P(0°)$, $P(45°)$, $P(90°)$, and $P(135°)$ represent the intensities of the four polarization directions

$$S_0 = P(0°) + P(90°) = P(45°) + P(135°) \tag{14}$$

$$S_1 = P(0°) - P(90°) \tag{15}$$

$$S_2 = P(45°) - P(135°). \tag{16}$$

III. Experiments on Dataset

To verify the feasibility of our approach, we first used the CAVE hyperspectral dataset [40] for simulation. The CAVE dataset contains images of various artificial scenes with a spectral range of 400–700 nm, a spectral resolution of 10 nm, and a spatial resolution of 512 × 512 pixels. To achieve super-resolution of the spectral information for the notch-filtered image, it is necessary to extract the spectral features of the captured scene spectral data cubes. Therefore, a hyperspectral image of a scene in the CAVE dataset was selected as the training set. Since the spectral features of adjacent pixels are similar in most cases, the training set was downsampled by a factor of 4 in the spatial domain. To expand the representation and generalization ability of the spectral feature dictionary, the selected training set must include as many spectral feature types as possible. Here, we used the K-times singular value decomposition (K-SVD) algorithm to train the spectral feature dictionary.

To quantitatively evaluate the spectral super-resolution results of the proposed method, three different metrics were

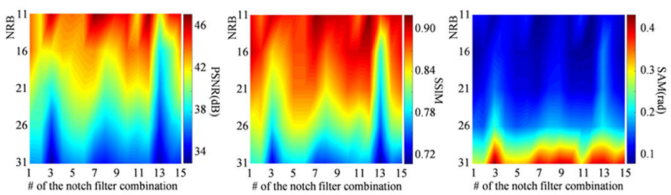

Fig. 6. Effects of different NBR and different notch filter combinations on the reconstructed multispectral image results. The number of the notch filter combination corresponds to the number of the notch filter combination in Table II.

used: peak SNR (PSNR), structure similarity index measure (SSIM), and spectral angle mapping (SAM). On the one hand, PSNR and SSIM were used to assess the spatial fidelity of the images reconstructed by the proposed method. Higher values of PSNR and SSIM indicate better reconstruction fidelity. On the other hand, SAM was applied to describe the spectral fidelity of the reconstructed images. A smaller value of SAM indicates a lower error in the reconstructed spectral images.

For the simulation, the center wavelengths of the notch filters were selected depending on the commercially available notch filters and the spectrum of the CAVE dataset. On one side, the variety of commercial notch filters is limited to the range of 480–630 nm, with only five different center wavelengths. On the other side, the overcomplete dictionary used in this research was trained based on the CAVE dataset with a spectral range of 400–700 nm. Therefore, to conduct the simulation and experiments, we used five different types of notch filters with center wavelengths of 488, 514, 532, 561, and 632 nm. Based on the spectral transmission rate curve of these notch filters, the CAVE dataset was used to simulate images acquired by a multiaperture camera array through different notch filters.

Fig. 6 shows the effect of the number of bands of the reconstructed multispectral image (NBR) and the different filter combinations on the spectral super-resolution reconstruction results. As shown in Fig. 6(a) and (b), the quality of the spectral super-resolution reconstruction significantly decreased with increasing NBR. In contrast, Fig. 6(c) indicates that the SAM of the spectral super-resolution reconstruction increased when the NBR was reduced to a certain extent. One reason for this phenomenon was the effect of notch filter combination selection. When the NBR was small, the center wavelength of most of the reconstructed spectral images was far away from the center wavelength of the selected notch filter. This yielded consistent notch image and panchromatic image data, which conversely affected the coherence between the acquisition matrix and the dictionary. To balance the number of recovered bands and the accuracy of the reconstructed spectral super-resolution image, the NBR was set to 16 in all subsequent experiments.

There are 15 possible combinations of notch filters, as shown in Table II, which are limited by the available types of commercial notch filters. All 15 combinations were simulated, and the proposed spectral super-resolution reconstruction method was used to find the optimal filter combination. PAN refers to an aperture not covered with a notch

TABLE II

NOTCH FILTER COMBINATIONS TESTED IN THE SIMULATIONS USING THE CAVE DATASET. THE DIFFERENT NOTCH FILTER COMBINATIONS WERE QUANTITATIVELY EVALUATED BY THREE METRICS: PSNR, SSIM, AND SAM. THE SIMULATION RESULTS WERE OBTAINED FROM THE PROPOSED SPECTRAL SUPER-RESOLUTION RECONSTRUCTION METHOD. NBR REPRESENTS THE NUMBER OF BANDS OF THE RECONSTRUCTED MULTISPECTRAL IMAGE

#	Center Wavelength (nm)					Result		
	Sub-aperture 1	Sub-aperture 2	Sub-aperture 3	Sub-aperture 4	NRB	PSNR (dB)	SSIM	SAM (rad)
1	PAN	488	532	632	16	44.065	**0.898**	**0.072**
2	PAN	488	561	632	16	41.973	0.882	0.086
3	PAN	514	532	561	16	42.039	0.844	0.118
4	PAN	514	532	632	16	42.882	0.850	0.113
5	PAN	514	561	632	16	42.713	0.868	0.094
6	PAN	532	561	632	16	43.203	0.868	0.094
7	488	532	561	632	16	42.017	0.859	0.100
8	514	532	561	632	16	43.441	0.888	0.076
9	PAN	488	514	532	16	42.507	0.876	0.110
10	PAN	488	514	561	16	44.214	0.891	0.079
11	PAN	488	514	632	16	43.786	0.894	0.074
12	PAN	488	532	561	16	**44.493**	0.895	0.077
13	488	514	532	561	16	37.979	0.785	0.159
14	488	514	532	632	16	39.988	0.866	0.100
15	488	514	561	632	16	43.165	0.888	0.075

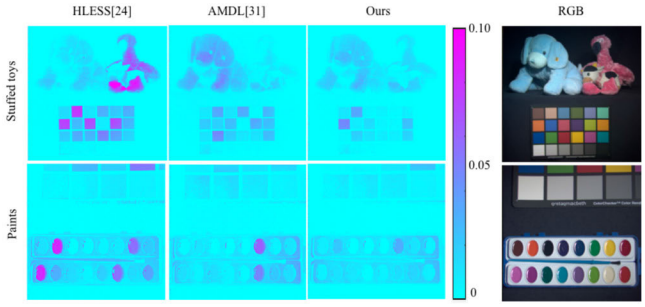

Fig. 7. Error maps of the 550-nm spectral image obtained from different spectral super-resolution methods.

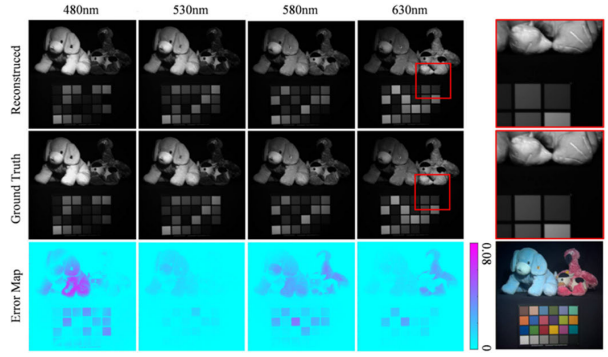

Fig. 8. First notch filter combination in Table III was simulated, 4 out of the 16 reconstructed spectral images of the "Stuffed toys" scene are selected and displayed. The first and second rows show the spectral super-resolution reconstruction results and the ground-truth spectral images, respectively. The third row shows the error image.

filter, which was only used to acquire monochrome images. In addition, Fig. 6 shows that the number of reconstructed spectral images significantly affected their imaging quality. Hence, the tradeoff between PSNR, SSIM, and SAM must be balanced considering the spectral resolution and the image

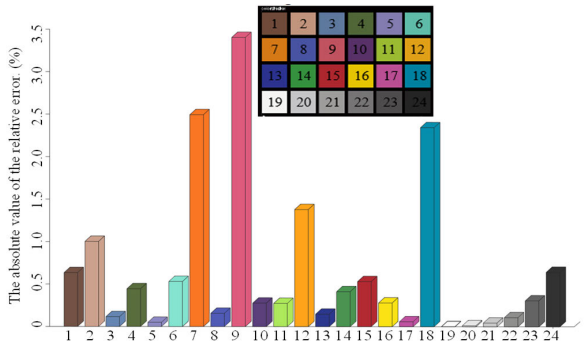

Fig. 9. Absolute error for the 24 color patches in the "stuffed toys" scene.

quality of the reconstructed spectrum. In this case, the number of reconstructed bands was set to 16.

For a similar NBR, the quality of spectral super-resolution reconstruction results was affected by the notch filter combination because the corresponding center wavelength distribution directly affects the measurement matrix of the multiaperture imaging system. The lower the correlation between the measurement matrix and the spectral feature dictionary, the better the computational results [41]. Considering the NBR and the quality of the multispectral image, the first notch filter combination (PAN, 488, 532, and 632 nm) in Table II was more suitable for high-quality multispectral image reconstruction than the other groups of notch filters. Therefore, this group of notch filters was used for indoor tests and field tests in subsequent experiments.

Table III compares the proposed and other spectral super-resolution methods. To ensure an accurate and fair comparison and demonstrate the performance of our proposed method, the different methods were applied to the images collected by the notch-filter-based spectral imaging system. As shown in Table III, the proposed method outperformed the other spectral super-resolution methods, namely, HLESSI [24] and

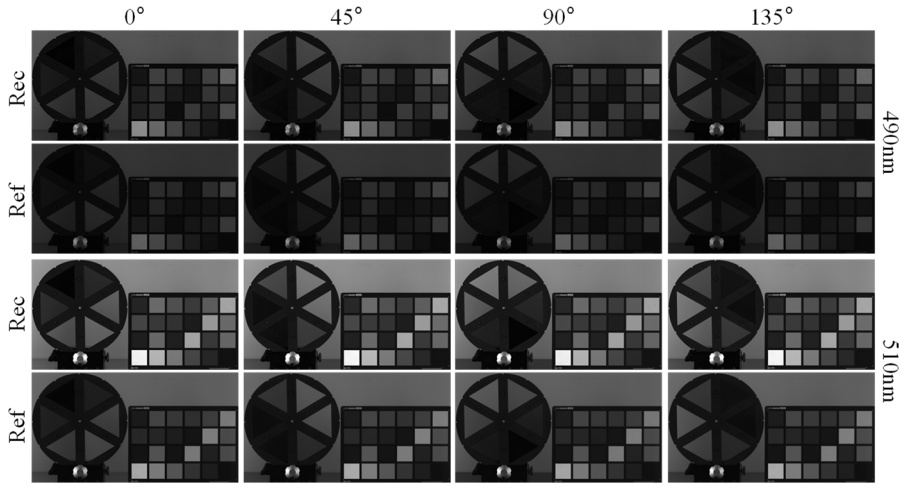

Fig. 10. Spectral super-resolution was performed on the panchromatic and notch-filtered polarization images (488, 532, and 632 nm) collected by the proposed four-aperture imaging system. The imaging targets are polarized targets and a color checker. Rows 1 and 2 show images for the four polarization directions at a wavelength of 490 nm. Rows 3 and 4 show images for the four polarization directions at a wavelength of 510 nm. "Rec" represents the spectral super-resolution image reconstructed by the proposed method, and "Ref" represents the reference image captured by a polarization camera and a bandpass filter of the corresponding wavelength.

TABLE III

IMAGES ACQUIRED BY OUR SYSTEM WERE SIMULATED USING THE CAVE PUBLIC DATASET, AND SPECTRAL SUPER-RESOLUTION RECONSTRUCTIONS WERE PERFORMED USING DIFFERENT SPECTRAL SUPER-RESOLUTION METHODS FOR COMPARISON. THE MEAN PSNR/SSIM/SAM OF THE MULTISPECTRAL IMAGE SUPER-RESOLUTION RESULTS WERE CALCULATED. THE SPECTRAL RANGE OF THE MULTISPECTRAL IMAGE SUPER-RESOLUTION RECONSTRUCTION RESULTS IS 480–630 nm, AND THE BANDWIDTH OF A SINGLE SPECTRAL IMAGE IS 10 nm. ALL SIMULATED CAPTURED IMAGE DATA WERE GENERATED ACCORDING TO THE FIRST NOTCH FILTER COMBINATION (PAN, 488, 532, AND 632 nm)

Methods	PSNR	SSIM	SAM
HLESSI [24]	36.70	0.84	0.13
AMDL [31]	43.01	0.89	0.09
Ours	**44.17**	**0.90**	**0.07**

AMDL [31]. Fig. 7 shows the error maps obtained from different spectral super-resolution methods. The method in [24] and [31] produced evidently larger errors, which can be attributed to [24] using only the prior of spectral smoothness and [31] only the prior of sparsity for spectral data reconstruction. The results indicate that the combination of sparsity and smoothness, as described in Section II, can help better recover spectral data.

Table IV shows the simulation results of the first notch filter combination (PAN, 488, 532, and 632 nm) for 32 scenarios in the CAVE dataset. Our method can be used to obtain 16-band spectral super-resolution images with average PSNR, SSIM, and SAM of 44.07 dB, 0.90, and 0.07 rad, respectively.

The reconstruction results of the "stuffed toys" scene in the CAVE dataset were further analyzed. Fig. 8 shows the comparison between the spectral super-resolution results of the proposed method and the ground-truth image. The normalized error image shows that the absolute error on a single pixel is in the interval [0, 0.08]. Fig. 9 shows the absolute error for 24 different color patches in the "stuffed toys" scene, with an average of 0.68%. Moreover, the average value of the SAM indicator was 0.06 rad. It can be seen that the calculation results for some color blocks have large errors, which can be attributed to the fact that the training set contains only a small proportion of data with similar colors.

IV. EXPERIMENTS ON REAL CAPTURED DATA

A. Laboratory Experiments

In Section III, the CAVE dataset was used to verify the feasibility of the proposed spectral super-resolution method. However, due to the lack of public multispectral-polarization datasets, it is not possible to directly verify whether the spectral super-resolution method is applicable to polarization images. Instead, we used field experiments to directly verify whether the multispectral-polarization image after spectral super-resolution still retains the polarization information of the target scene.

Table II shows that when the present system was equipped with the first set of notch filters, the 16-band spectral images can be recovered after spectral super-resolution using the proposed algorithm. Concurrently, indicators, such as PSNR, SSIM, and SAM, can be optimized. Therefore, the first set of notch filters (PAN, 488, 532, and 632 nm) was used for indoor imaging experiments. The targets used include a color-checker (X-rite) and a polarized target, as shown in Fig. 10. The polarized target was composed of six linear polarizers forming a disk. The directions of adjacent linear polarizers differed by 30°, which was used to analyze whether accurate polarization information is still retained in the spectral images obtained after spectral super-resolution. To verify the fidelity of the spectral information and the accuracy of the

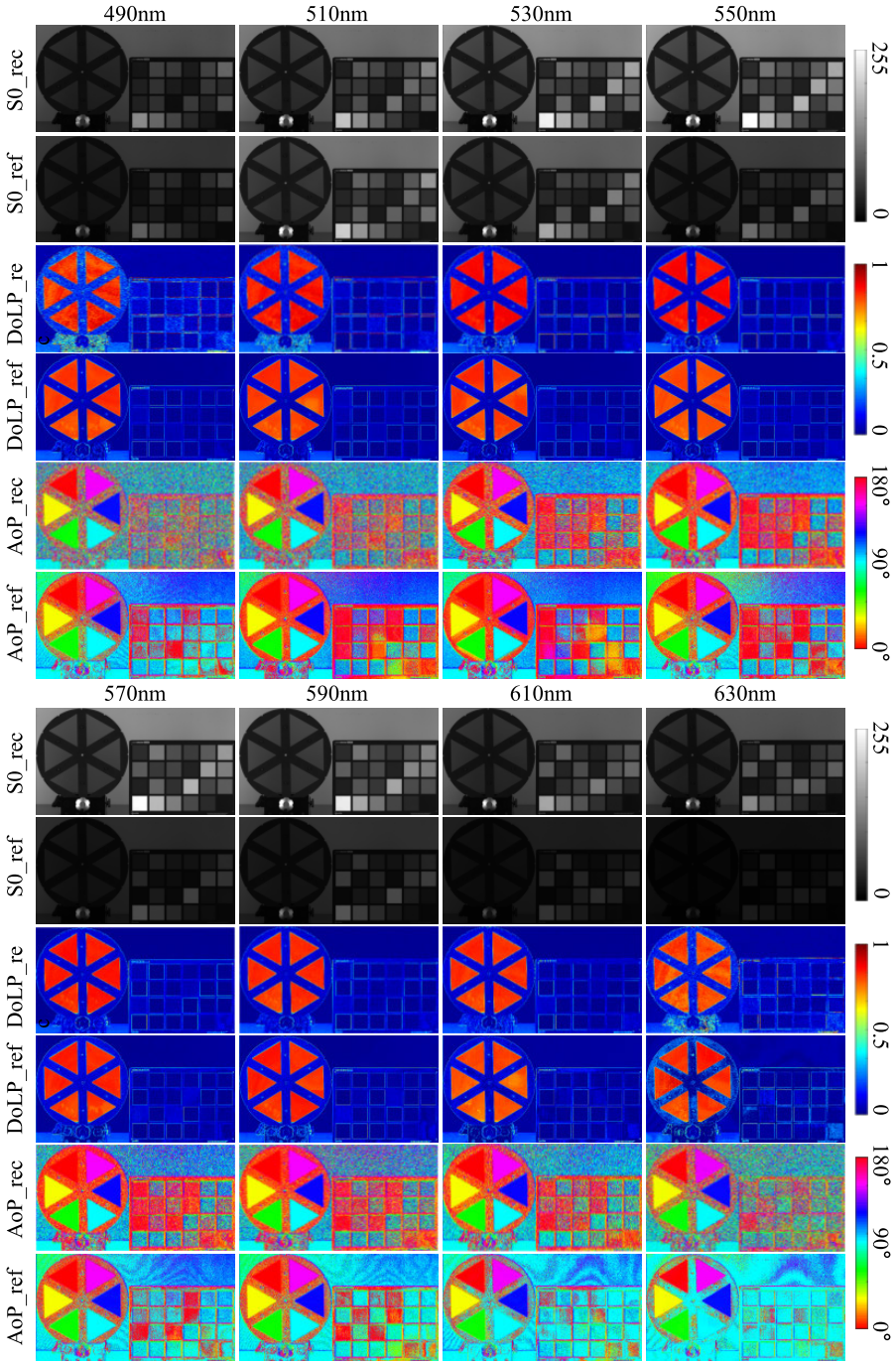

Fig. 11. Comparison of the imaging results obtained using the proposed method with those obtained using the bandpass filter and polarizing camera at wavelengths of 490, 510, 530, 550, 570, 590, 610, and 630 nm. Suffixes "Rec" and "Ref" indicate that the image was obtained using the proposed spectral super-reconstruction method or using the polarization camera and the corresponding bandpass filter, respectively.

polarization information of the reconstructed multispectral-polarization image, we installed a bandpass filter (Thorlabs, FB480-10-FB630-10) in front of a polarization camera of the same model. The same target scene was then photographed for comparison.

After registering the images with the four-aperture imaging system, the notch-filtered images were processed using the spectral super-resolution algorithm. In Fig. 10, the pictures in rows 1 and 3 show the multispectral images obtained at four different polarization states (490- and 510-nm wavelengths). The calculated spectral images were compared with reference images captured using a bandpass filter and a polarizing camera, which correspond to rows 2 and 4 in Fig. 10.

The S0 image of the target scene can be obtained using (14). Rows 1 and 7 in Fig. 11 are the multispectral S0 images obtained by the method in this work. The images in rows 2 and 8 are multispectral S0 images obtained with a bandpass filter and a polarization camera. The corresponding DoLP images

TABLE IV

USING THE FIRST NOTCH FILTER COMBINATION, THE PROPOSED METHOD IS SIMULATED AND VERIFIED BY USING THE SPECTRAL DATA CUBE OF 32 SCENARIOS IN THE CAVE PUBLIC DATASET. THE PSNR, SSIM, AND SAM INDICATORS OF EACH SCENE ARE SHOWN IN THE TABLE. THE AVERAGE VALUES OF PSNR, SSIM, AND SAM INDICATORS ARE 44.07 dB, 0.90, AND 0.07 rad, RESPECTIVELY

Items \ Metrics	PSNR (dB)	SSIM	SAM (rad)	Items \ Metrics	PSNR (dB)	SSIM	SAM (rad)
Balloons	41.65	0.86	0.07	Feathers	41.74	0.90	0.08
Beads	32.10	0.93	0.15	Flowers	46.63	0.82	0.09
CD	36.07	0.89	0.07	Glass tiles	38.18	0.95	0.08
Chart, toy	42.05	0.90	0.07	Hairs	52.61	0.95	0.06
Clay	35.05	0.79	0.14	Jelly beans	43.12	0.97	0.07
Cloth	49.83	0.99	0.03	Oil painting	47.17	0.98	0.05
Statue	48.53	0.76	0.11	Paints	42.66	0.92	0.05
Face	46.97	0.88	0.06	Photo, face	44.10	0.84	0.09
Beers	44.48	0.91	0.03	Pompoms	36.68	0.96	0.10
Food	45.09	0.91	0.07	Apples	54.56	0.85	0.06
Lemon slice	50.02	0.96	0.05	Peppers	47.03	0.88	0.06
Lemons	51.12	0.90	0.06	Sponges	35.01	0.88	0.06
Peppers	43.80	0.88	0.07	Stuffed toys	41.94	0.82	0.07
Strawberries	50.99	0.90	0.06	Superballs	37.92	0.92	0.11
Sushi	48.17	0.94	0.06	Thread spools	45.45	0.94	0.07
tomatoes	48.55	0.80	0.07	Water colors	40.82	0.95	0.05

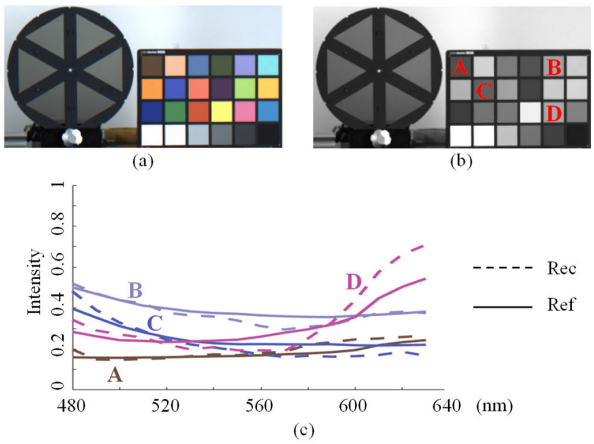

Fig. 12. Reconstructed value of the spectral curve on the A, B, C, and D color patches compared with the reference value. Suffixes "Rec" and "Ref" indicate that the image was obtained using the proposed spectral super-reconstruction method or using the polarization camera and the corresponding bandpass filter, respectively.

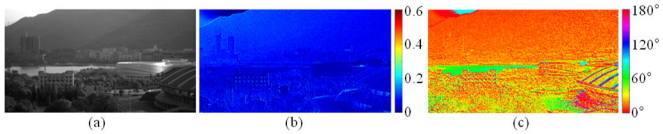

Fig. 13. Outdoor Scene 1 was photographed using a panchromatic polarization camera without any optical filters: (a) S0 image, (b) DoLP calculated using (13), and (c) AoP calculated using (12).

and AoP images are in rows 3–6 and 9–12, respectively, which can be obtained by (12) and (13).

Fig. 11 clearly shows that the proposed method retains the polarization information of the target scenes acquired through polarization cameras while realizing the reconstructed spectral super-resolution images. Fig. 12 shows the spectral curves of the four regions on the color checker in the scene. It is

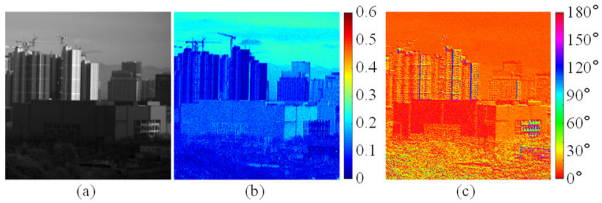

Fig. 14. Outdoor Scene 2 was photographed using a panchromatic polarization camera without any optical filters: (a) S0 image, (b) DoLP calculated using (13), and (c) AoP calculated using (12).

worth noting that the average SAM of the 24 color blocks in the color checker is 0.13 rad. The images of some bands in Figs. 11 and 12 have spectral or polarization distortions. This was because the spectral images of some wavelengths in the training set had low light intensities, so the trained dictionary did not perform well in these spectral wavelength ranges.

In addition, due to the difference in the field of view between the imaging apertures, it was required that image registration was performed and that the polarization information contained in the image acquired by the polarization detector remained unchanged during the registration operation. The homography matrix in the registration process will indirectly change the polarization state distribution on the focal plane of the polarization camera. One of the solutions would be to first divide the collected polarization image into subimages at 0°, 45°, 90°, and 135° and then perform image registration separately.

B. Field Experiments

Laboratory experiments showed that the proposed system can perform spectral super-resolution while preserving polarization information. Furthermore, the imaging system was tested in an outdoor natural scenario to verify its performance. At present, the polarization sensor combines a focal plane

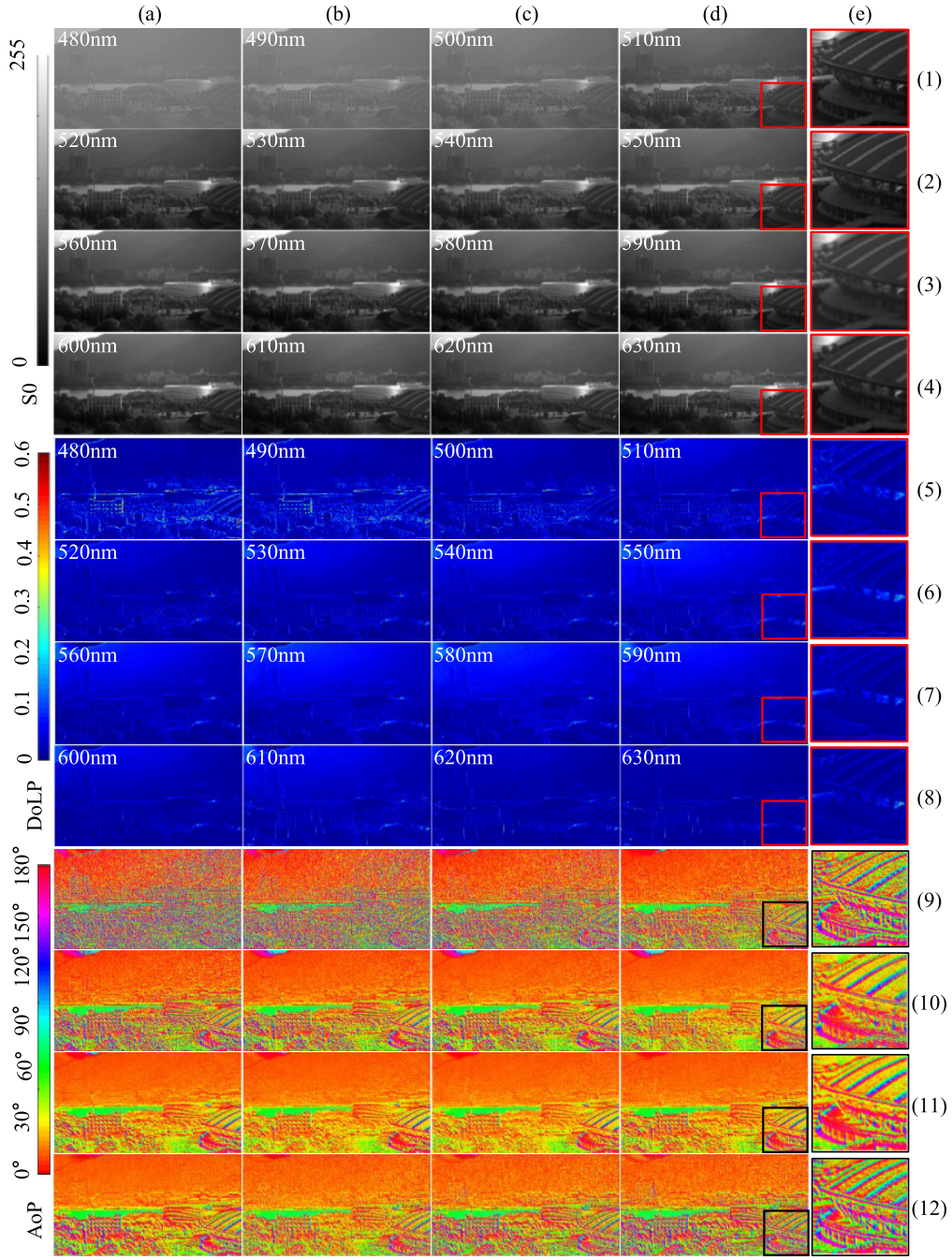

Fig. 15. Panchromatic polarization image and notch filter polarization images (488, 532, and 632 nm) were directly collected by the proposed system, and then, spectral super-resolution methods were performed on the polarization images. The S0, DoLP, and AoP images of 16 bands were reconstructed with a spectral range of 480–630 nm and a spectral resolution of 10 nm.

detector with a micropolarizer array, leading to the loss of light throughput and the decrease of the imaging SNR. Thus, the polarization information would be affected by the noise level. To address this issue, we have used the guided filtering method [42] for denoising the reconstructed images.

The direct imaging and calculation results for the natural scene are shown in Fig. 13. From the images captured by the panchromatic polarization camera and the spectral reconstruction results, the polarization characteristics exhibited by the lake, sky, buildings, and glass windows can be clearly seen. By calculating polarization properties such as DoLP and AoP, the target and background can be quickly distinguished. As shown in Figs. 13 and 14, the mountains, sky, and lake show different polarization characteristics. As shown in Fig. 15(e), the polarization characteristics display the contour information of buildings.

Figs. 14 and 15 show that the polarization characteristics of the buildings in the scene are clearly distinguished from those of the background. In the magnified area, the polarization characteristics of the glass windows on the buildings are also more prominent. In addition, even the same building will show different polarization characteristics depending on the angle of the reflected light. As depicted in Fig. 16, the analysis of the 16 reconstructed spectral images reveals that polarization

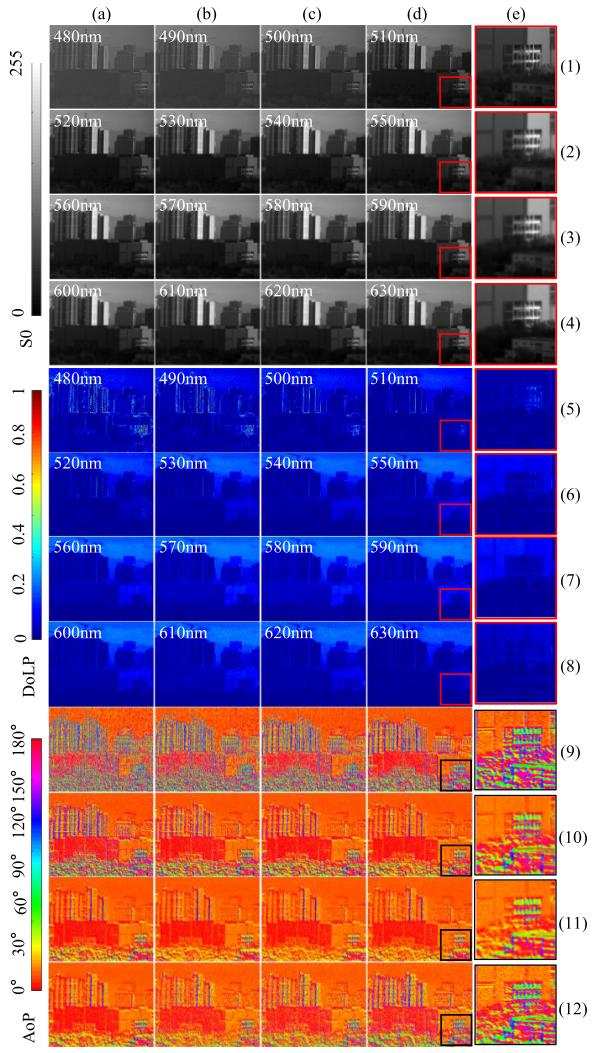

Fig. 16. Panchromatic polarization image and notch filter polarization images (488, 532, and 632 nm) were directly collected by the proposed system, and then, spectral super-resolution methods were performed on the polarization images. The S0, DoLP, and AoP images of 16 bands were reconstructed with a spectral range of 480–630 nm and a spectral resolution of 10 nm.

characteristics are influenced not only by the angle of the reflected light but also by various wavelength bands.

V. Conclusion

In this study, a light-efficient multispectral-polarization imaging system based on notch filters and a multiaperture imaging structure was proposed, and a prototype system was built for demonstration. The acquisition of multispectral-polarization images of a target scene can be achieved in one shot. The multiaperture multispectral-polarization imaging system combines the advantages of a snapshot polarization imaging sensor and those of a notch filter. This ensures that it can simultaneously capture multispectral and polarization images of the target scene with high spatial resolution. Systems using notch filters have the advantage of high light throughput, which shortens the required exposure time, resulting in higher frame rates for high-speed imaging. The proposed system outperformed conventional polarization imaging systems in terms of spectral and temporal resolutions. In this study, only four imaging apertures were used for polarized image acquisition, and three notch-filtered and one panchromatic polarization images were collected for computational imaging reconstruction. To improve the spectral resolution of the acquired data, a compressive sensing-based method was performed for spectral super-resolution. In the case of computational imaging reconstruction using three notch-filtered and one panchromatic polarized images, multispectral-polarization images of up to 16 spectral bands could be obtained. Furthermore, field experiments verified that the multispectral-polarization data cube after spectral super-resolution maintains the polarization information of the target scene. The proposed system confirms that the 2-D image sensor can be used to obtain high-dimensional, high-resolution, and high-quality optical information of the target scene.

In future work, we shall further investigate the improvement of the registration accuracy between images with different polarization states, to overcome the effect of the difference in the field of view between images acquired with different apertures. Moreover, a multispectral-polarization dataset needs to be established to study the method for improving the spectral super-resolution accuracy of multispectral-polarization images.

Acknowledgment

The authors would like to thank Dr. Pengfei Wang for his helpful advice and discussions.

References

[1] F. Huang, R. Cao, X. Wu, P. Lin, and B. Zhou, "High efficiency multi-spectral polarization imaging system," *Proc. SPIE*, vol. 12169, pp. 860–865, Mar. 2022.

[2] Y. Andre, J.-M. Laherrere, T. Bret-Dibat, M. Jouret, J.-M. Martinuzzi, and J.-L. Perbos, "Instrumental concept and performances of the POLDER instrument," *Proc. SPIE*, vol. 2572, pp. 79–90, Aug. 1995.

[3] J. Elders, H. Azene, G. Betraun, and K. Wilkerson, "Aerosol Polarimeter Sensor (APS) contamination control requirements and implementation," *Proc. SPIE*, vol. 7794, pp. 51–57, Sep. 2010.

[4] Y. Zhao, L. Zhang, and Q. Pan, "Spectropolarimetric imaging for pathological analysis of skin," *Appl. Opt.*, vol. 48, no. 10, pp. D236–D246, 2009, doi: 10.1364/AO.48.00D236.

[5] N. Li, Y. Zhao, Q. Pan, S. G. Kong, and J. C.-W. Chan, "Full-time monocular road detection using zero-distribution prior of angle of polarization," in *Proc. 16th Eur. Conf. Comput. Vis.*, Glasgow, U.K., Aug. 2020, pp. 457–473.

[6] Z. Li et al., "Directional polarimetric camera (DPC): Monitoring aerosol spectral optical properties over land from satellite observation," *J. Quant. Spectrosc. Radiat. Transf.*, vol. 218, pp. 21–37, Oct. 2018, doi: 10.1016/j.jqsrt.2018.07.003.

[7] D. J. Diner et al., "WindCam and MSPI: Two cloud and aerosol instrument concepts derived from Terra/MISR heritage," *Proc. SPIE*, vol. 7081, Aug. 2008, Art. no. 70810T.

[8] M. Garcia, C. Edmiston, R. Marinov, A. Vail, and V. Gruev, "Bio-inspired color-polarization imager for real-time in situ imaging," *Optica*, vol. 4, no. 10, pp. 1263–1271, Oct. 2017, doi: 10.1364/OPTICA.4.001263.

[9] A. Altaqui et al., "Mantis shrimp–inspired organic photodetector for simultaneous hyperspectral and polarimetric imaging," *Sci. Adv.*, vol. 7, no. 10, Mar. 2021, Art. no. eabe3196.

[10] J. S. Tyo, D. L. Goldstein, D. B. Chenault, and J. A. Shaw, "Review of passive imaging polarimetry for remote sensing applications," *Appl. Opt.*, vol. 45, no. 22, pp. 5453–5469, 2006.

[11] X. Wu, M. Pankow, H.-Y. S. Huang, and K. Peters, "High-speed polarization imaging of dynamic collagen fiber realignment in tendon-to-bone insertion region," *Proc. SPIE*, vol. 23, no. 11, 2018, Art. no. 116002.

[12] A. Balandra et al., "P-MIRU, a polarized-spectral imaging system, reveals reflection information on the biological surface," *Plant Cell Physiol.*, 2023, Art. no. pcad045. [Online]. Available: https://academic.oup.com/pcp/advance-articleabstract/, doi: 10.1093/pcp/pcad045.

[13] A. Fan et al., "Full-Stokes polarization multispectral images of various stereoscopic objects," *Sci. Data*, vol. 10, no. 1, p. 328, May 2023.
[14] S. Li, J. Jiao, and C. Wang, "Research on polarized multi-spectral system and fusion algorithm for remote sensing of vegetation status at night," *Remote Sens.*, vol. 13, no. 17, p. 3510, Sep. 2021.
[15] R. M. Azzam and K. A. Giardina, "Polarization analysis based on grating conical diffraction," *Proc. SPIE*, vol. 1746, pp. 2–13, May 1992.
[16] X. Liu, J. Chang, Y. Zhong, S. Feng, D. Song, and Y. Hu, "Optical design of a simultaneous polarization and multispectral imaging system with a common aperture," *J. Mod. Opt.*, vol. 67, no. 5, pp. 462–468, Mar. 2020.
[17] J. L. Pezzaniti and D. B. Chenault, "A division of aperture MWIR imaging polarimeter," *Proc. SPIE*, vol. 5888, pp. 239–250, Aug. 2005.
[18] F. Huang, C. Ke, X. Wu, S. Wang, J. Wu, and X. Wang, "Polarization dehazing method based on spatial frequency division and fusion for a far-field and dense hazy image," *Appl. Opt.*, vol. 60, no. 30, pp. 9319–9332, 2021.
[19] K. Shinoda and Y. Ohtera, "Alignment-free filter array: Snapshot multispectral polarization imaging based on a Voronoi-like random photonic crystal filter," *Opt. Exp.*, vol. 28, no. 26, pp. 38867–38882, 2020.
[20] K. Shinoda, Y. Ohtera, and M. Hasegawa, "Snapshot multispectral polarization imaging using a photonic crystal filter array," *Opt. Exp.*, vol. 26, no. 12, pp. 15948–15961, 2018.
[21] Y. Yao et al., "Single-shot real-time ultrafast imaging of femtosecond laser fabrication," *ACS Photon.*, vol. 8, no. 3, pp. 738–744, Mar. 2021.
[22] L. Gao and L. V. Wang, "A review of snapshot multidimensional optical imaging: Measuring photon tags in parallel," *Phys. Rep.*, vol. 616, pp. 1–37, Feb. 2016.
[23] K. G. Lore, K. K. Reddy, M. Giering, and E. A. Bernal, "Generative adversarial networks for spectral super-resolution and bidirectional RGB-to-multispectral mapping," in *Proc. IEEE/CVF Conf. Comput. Vis. Pattern Recognit. Workshops (CVPRW)*, Jun. 2019, pp. 926–933, doi: 10.1109/CVPRW.2019.00122.
[24] M. Zhang, L. Wang, L. Zhang, and H. Huang, "High light efficiency snapshot spectral imaging via spatial multiplexing and spectral mixing," *Opt. Exp.*, vol. 28, no. 14, pp. 19837–19850, Jul. 2020, doi: 10.1364/OE.393173.
[25] R. Huang, X. Li, and L. Zhao, "Incremental kernel non-negative matrix factorization for hyperspectral unmixing," in *Proc. IEEE Int. Geosci. Remote Sens. Symp. (IGARSS)*, Jul. 2016, pp. 6569–6572.
[26] L. Dong, Y. Yuan, and X. Luxs, "Spectral–spatial joint sparse NMF for hyperspectral unmixing," *IEEE Trans. Geosci. Remote Sens.*, vol. 59, no. 3, pp. 2391–2402, Mar. 2021.
[27] C. Tao et al., "Compressive single-pixel hyperspectral imaging using RGB sensors," *Opt. Exp.*, vol. 29, no. 7, pp. 11207–11220, Mar. 2021, doi: 10.1364/OE.416388.
[28] B. Arad and O. Ben-Shahar, "Sparse recovery of hyperspectral signal from natural RGB images," in *Proc. 14th Eur. Conf. Comput. Vis. (ECCV)*. Amsterdam, The Netherlands: Springer, Oct. 2016, pp. 19–34.
[29] J. Li, S. Du, R. Song, C. Wu, Y. Li, and Q. Du, "HASIC-Net: Hybrid attentional convolutional neural network with structure information consistency for spectral super-resolution of RGB images," *IEEE Trans. Geosci. Remote Sens.*, vol. 60, 2022, Art. no. 5522515.
[30] T. Panther, M. Schambach, and M. Heizmann, "Improving light efficiency in multispectral imaging via complementary notch filters," *Proc. SPIE*, vol. 11787, Jun. 2021, Art. no. 117870K.
[31] F. Huang, P. Lin, X. Wu, R. Cao, and B. Zhou, "Compressive sensing-based super-resolution multispectral imaging system," *Proc. SPIE*, vol. 12169, pp. 755–760, Mar. 2022.
[32] J. Tanida et al., "Thin observation module by bound optics (TOMBO): Concept and experimental verification," *Appl. Opt.*, vol. 40, no. 11, pp. 1806–1813, Apr. 2001, doi: 10.1364/AO.40.001806.
[33] A. Wagadarikar, R. John, R. Willett, and D. Brady, "Single disperser design for coded aperture snapshot spectral imaging," *Appl. Opt.*, vol. 47, no. 10, pp. B44–B51, 2008.
[34] J. Bacca, Y. Fonseca, and H. Arguello, "Compressive spectral image reconstruction using deep prior and low-rank tensor representation," *Appl. Opt.*, vol. 60, no. 14, pp. 4197–4207, 2021.
[35] M. E. Gehm, R. John, D. J. Brady, R. M. Willett, and T. J. Schulz, "Single-shot compressive spectral imaging with a dual-disperser architecture," *Opt. Exp.*, vol. 15, no. 21, pp. 14013–14027, 2007.
[36] P. Wang, L. Wang, H. Leung, and G. Zhang, "Super-resolution mapping based on spatial–spectral correlation for spectral imagery," *IEEE Trans. Geosci. Remote Sens.*, vol. 59, no. 3, pp. 2256–2268, Mar. 2021.
[37] S. Boyd, N. Parikh, E. Chu, B. Peleato, and J. Eckstein, "Distributed optimization and statistical learning via the alternating direction method of multipliers," *Found. Trends Mach. Learn.*, vol. 3, no. 1, pp. 1–122, 2010.
[38] H. Bay, T. Tuytelaars, and L. Van Gool, "SURF: Speeded up robust features," in *Proc. 9th Eur. Conf. Comput. Vis. (ECCV)*, Graz, Austria. Berlin, Germany: Springer, 2006, pp. 404–417.
[39] V. Gruev, R. Perkins, and T. York, "CCD polarization imaging sensor with aluminum nanowire optical filters," *Opt. Exp.*, vol. 18, no. 18, pp. 19087–19094, 2010, doi: 10.1364/OE.18.019087.
[40] F. Yasuma, T. Mitsunaga, D. Iso, and S. K. Nayar, "Generalized assorted pixel camera: Postcapture control of resolution, dynamic range, and spectrum," *IEEE Trans. Image Process.*, vol. 19, no. 9, pp. 2241–2253, Sep. 2010.
[41] C. D. Sigg, T. Dikk, and J. M. Buhmann, "Learning dictionaries with bounded self-coherence," *IEEE Signal Process. Lett.*, vol. 19, no. 12, pp. 861–864, Dec. 2012.
[42] K. He, J. Sun, and X. Tang, "Guided image filtering," *IEEE Trans. Pattern Anal. Mach. Intell.*, vol. 35, no. 6, pp. 1397–1409, 2012.

Feng Huang was born in Fuzhou, China, in 1979.

He is currently with the School of Mechanical Engineering and Automation, Fuzhou University, Fuzhou, China. His research interest includes optoelectronic imaging.

Rongjin Cao received the B.S. degree from Fuzhou University, Fuzhou, China, in 2019, where he is currently pursuing the master's degree with the School of Mechanical Engineering and Automation.

His research interests include computational imaging and visible multispectral-polarization imaging.

Peng Lin received the B.S. degree from the Nanjing University of Science and Technology, Nanjing, China, in 2019. He is currently pursuing the master's degree with the School of Mechanical Engineering and Automation, Fuzhou University, Fuzhou, China.

His research interests include computational imaging and visible multispectral-polarization imaging.

Bin Zhou received the B.S. degree from Fuzhou University, Fuzhou, China, in 2018, where he is currently pursuing the master's degree with the School of Mechanical Engineering and Automation.

His research interests include computational imaging and infrared nondestructive testing.

Xianyu Wu received the master's and Ph.D. degrees in mechanical engineering from North Carolina State University, Raleigh, NC, USA.

His research laboratory specializes in advancing the fundamental principles of optical sensing and imaging within precision measurement systems. He is particularly passionate about developing cutting-edge optical measurement and imaging systems that seamlessly integrate advancements in both hardware and software. Their collective efforts are aimed at pushing the boundaries of optical technology to address real-world challenges and provide innovative solutions.